

# Effect of microstructure on hydrogen absorption in WMoTaNbV high-entropy alloy

Anna Liski <sup>a,\*,</sup>, Marianna Kemell <sup>b,</sup>, Tomi Vuoriheimo <sup>a,</sup>, Ko-Kai Tseng <sup>c,</sup>, Ting-En Shen <sup>c,</sup>,  
Che-Wei Tsai <sup>c,d,</sup>, Jien-Wei Yeh <sup>c,d,</sup>, Kenichiro Mizohata <sup>a,</sup>

<sup>a</sup> Department of Physics, University of Helsinki, P.O. Box 43, 00014, Helsinki, Finland

<sup>b</sup> Department of Chemistry, University of Helsinki, P.O. Box 55, 00014, Helsinki, Finland

<sup>c</sup> Department of Materials Science and Engineering, National Tsing Hua University, Hsinchu 30013, Taiwan, ROC

<sup>d</sup> High Entropy Materials Center, National Tsing Hua University, Hsinchu 30013, Taiwan, ROC

## ARTICLE INFO

### Keywords:

High entropy alloy

Grain

Topography

Hydrogen

SEM

EDS

Elastic recoil

## ABSTRACT

The refractory high entropy alloy, WMoTaNbV, absorbs significant quantities of H directly from the atmosphere. The effective hydrogen absorption has been attributed to the elemental composition of the alloy as well as its highly elaborate lattice structure. In this work, we apply scanning electron microscopy and ion beam analysis tools to investigate the effect of grain size and morphology on hydrogen storage, observing a consistency between the microstructure of WMoTaNbV alloy and hydrogen absorption.

## 1. Introduction

The extreme conditions inside a tokamak fusion vessel affect the plasma facing wall, limiting the options for structural materials to pure W, in the regions with the most severe temperature and radiation loads, such as divertor. However, the environments inside the vessel are not uniform leaving the blanket – accommodating systems for tritium breeding and heat extraction – subjected to much lower temperatures [1]. In this part the material options widen to include steels and various alloys.

Refractory high-entropy alloys are a class of metallic alloys built on random ordering of multiple main components in single crystal phase and they outperform many of the high-performance superalloys at high temperatures [2]. The alloy made of W-Mo-Ta-Nb-V elements displays exceptional mechanical durability, high irradiation tolerance and good thermal conductivity [3]. Our previous studies have demonstrated the alloy absorbing high levels of hydrogen from the atmosphere over a time period of several weeks [4]. Although the large hydrogen retention is unfavorable considering fusion applications the alloy displays a greater response to the hydrogen removal strategies in its surface layers as compared to tungsten [5]. The hydrogen retention could therefore be potentially managed by crafting the layer thickness.

Hydrogen has a high detrapping energy ( $1.7 \pm 0.8$  eV) from WMoTaNbV alloy, but has a strong response for isotopic exchange in

the surface regions (<400 nm), switching significant part of implanted deuterium to hydrogen during gas annealing at temperatures as low as 200 °C [4,5]. The high capacity for hydrogen retention arises from the elemental composition of WMoTaNbV alloy, as it is partially composed of hydrogen absorbing group-V elements — Nb, V and Ta. These elements hold negative solution enthalpies for hydrogen that lead to spontaneous absorption from the atmosphere [6]. The energy of hydrogen trapping in WMoTaNbV lattice is influenced by the degree of lattice distortion [7]. The strains in the lattice create a variety of potential trapping sites for the hydrogen atom to occupy, rising the maximum retention capacity [8]. The microstructural characteristics are likely to have an effect of hydrogen storage, as they often are accompanied by stresses and tension. In BCC metals, hydrogen has been observed to accumulate in the zones affected by plastic deformation and areas with elevated stress/strain, e.g. crack tips [9]. This work takes a closer look at the microstructure and elemental composition of WMoTaNbV alloy, finding a connection between the levels of hydrogen retention and the grain structure.

## 2. Materials and methods

### 2.1. Sample preparation

The equimolar WMoTaNbV alloy was casted by vacuum arc melting

\* Corresponding author.

E-mail address: [anna.liski@helsinki.fi](mailto:anna.liski@helsinki.fi) (A. Liski).

<https://doi.org/10.1016/j.nme.2025.101870>

Received 3 June 2024; Received in revised form 30 December 2024; Accepted 6 January 2025

Available online 12 January 2025

2352-1791/© 2025 The Authors. Published by Elsevier Ltd. This is an open access article under the CC BY-NC license (<http://creativecommons.org/licenses/by-nc/4.0/>).

at the High Entropy Materials Center of National Tsing Hua University [10]. The casting formed an alloy with a BCC solid solution phase as confirmed with X-ray diffraction measurement [10]. The grain size of the alloy has been observed to be heavily dependent on the rate of cooling [11]. The grains showed a dendritic structure under scanning electron microscopy (SEM) combined with a microscale elemental segregation where the centers of the grains were enriched with W and the boundaries with V, Nb and Mo [3]. The sample pieces ( $5 \times 5 \times 1 \text{ mm}^3$ ) were polished to a reflective surface with diamond suspension, lowering the polishing particle size down to 50 nm. The polished samples were then annealed for 2 h and 24 h in a quartz tube oven with vacuum of  $10^{-7}$  mbar at 1000 °C to release the hydrogen stored in the material. After the release, the samples were left in the ambient air for a year to allow hydrogen re-absorption from the atmosphere. The time period was long enough to reach an equilibrium concentration in the annealed samples.

## 2.2. Topographical and elemental characterization

The surface topography and the elemental composition of the alloy was studied with Hitachi S-4800 field emission scanning electron microscope (FESEM) equipped with an Oxford INCA350 EDX spectrometer. Elemental concentrations were quantified from EDS obtaining an average composition of Mo (20.7 at-%), Nb (20.3 at-%), Ta (20.4 at-%), V (19.2 at-%) and W (19.4 at-%) [4]. The quantities were obtained by using the following emission x-ray lines, W: ( $L\alpha$ ), Mo: ( $L\alpha$ ), Nb: ( $L\alpha$ ), V: ( $K\alpha$ ), Ta: ( $L\alpha$ ). The lateral resolution of 20 keV electrons used in the measurements was  $\sim 0.5 \mu\text{m}$ , the interaction volume is pictured in Fig. 1.

## 2.3. Elastic recoil detection analysis

The concentrations of H in each WMoTaNbV alloy samples were measured with Elastic Recoil Detection Analysis (ERDA). An incident ion of  $^{28}\text{Si}^{5+}$  was used with the energy of 24 MeV. The incident angle was set to 30° and the detector positioned to 25° from the sample surface, achieving a depth profiling of up to 400 nm with the configuration. The distance between the sample and the detector was 40 mm and the solid angle limited to  $2 \times 7 \text{ mm}^2$ . The detector had a nominal energy resolution of 15 keV. Heavier particles were stopped at the entrance of detector with 4  $\mu\text{m}$  havar foil. The secondary electrons were suppressed with a metal net, with voltage of  $-300 \text{ V}$ . The data was collected over the period of 10 min and the current was kept  $\sim 35 \text{ pA}$  to reduce temperature changes in the process. The measured data was analyzed for time dependency, finding a deviation of 4.6%, 1.8%, 3.9% in the hydrogen yield around the mean over the measurement period, for 0 h, 2 h and 24 h annealed samples, respectively. The variance is considered in the error margins of the obtained concentration values.

## 3. Results and discussion

### 3.1. Topography and composition of grain boundaries

The microscopy reveals a smooth landscape with dents covering the surface of the sample. The dents are located in the grain intersections, originating from the inherent porosity of the sample bulk. The size of the intergranular pores was in the order of tens of microns, as estimated from scanning electron microscopy images. With further magnification, the pores are observed to have textured surface structures on their inner parts which were not subjected to abrasion during polishing. The textures were spherical formations of  $\sim 200 \text{ nm}$  covering the inner surfaces of the pores with even density. The formations are pictured in Fig. 2. In the figure, the top row depicts an example of the size scales of the objects as the pore and the spherical formations within are presented with increasing magnification. The middle row of the Fig. 2 pictures similar formations as observed in each sample of WMoTaNbV

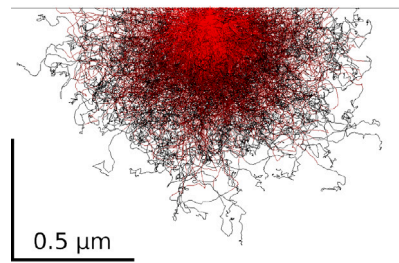


Fig. 1. The scattering of electrons ( $E_e = 20 \text{ keV}$ ) in WMoTaNbV alloy. The simulation was done with Monte Carlo Simulation software by Kimio Kanda, Hitachi, 1996.

alloy – 0 h, 2 h and 24 h annealed – from left to right, respectively. Similar order is applied to the bottom row of the Fig. 2, picturing the grain structures of samples. The differences in microstructure of the samples are likely originating from different cooling rates during preparation process as the samples originate from different batches. The size of grains in the 2 h sample annealed is significantly smaller as to the one compared with the reference or to sample exposed to 24 h annealing. The annealed samples were cooled with a similar rate following the annealing at 1000 °C. This suggests that the observed differences in their grain size originate from manufacturing process rather than recrystallization of the samples during the annealing. The work of Ref. [11] has studied the temperature related properties of WMoTaNbV alloy, reaching a conclusion of temperatures below 1400 °C to be insufficient for inducing recrystallization. Moreover, as the middle row in the Fig. 2 shows, the textured grain surfaces appear in each of the samples and their appearance is not affected by the annealing process. The spherical formations are therefore most likely created during the casting of WMoTaNbV alloy.

Closer investigation of composition of the spherical formations presents a challenge as their size scale is below the spatial resolution limit of EDS point measurements. The formations are observed exclusively on the grain surfaces and are likely to be composed of one or more elements of the alloy enriching the grain boundary. These elements are V, Nb and Mo, as first observed in Ref. [11]. The segregation occurs during solidification, as the constituents crystallize at different temperatures. The grain nucleates from the solidification of W, capturing it as the most prominent element in the grain center. In contrary, the element with the lowest melting temperature solidifies last leaving the grain boundaries enriched with V [3]. In metals, recrystallization is typically observable at temperatures of  $0.3 T_m - 0.5 T_m$ . Pure metals often display smaller recrystallization temperatures, while alloys tend to need relatively higher temperatures, as compared to their melting temperature ( $T_m$ ). To ensure that the annealing temperature of 1000 °C does not cause mobilization of the V atoms in the alloy, the elemental compositions of the grains were studied. The mobilization of V would create differences in the composition between samples exposed to different durations of annealing.

To study the composition, we have performed a series of energy dispersive spectroscopy (EDS) measurements to obtain elemental mappings in WMoTaNbV alloy. The elemental maps were measured to study the compositions of the sample annealed for 24 h for 1000 °C and the un-annealed reference. The elemental maps are presented in Fig. 3. The figure displays a consistency between previous works with the accumulation of W to the middle parts of the grain, Ta forming a uniform distribution throughout the grain while the rest of the constituents populate the boundary [3]. The intensity of the color scales in the Fig. 3 are qualitative and the comparison between measurements performed on different samples should be made with reservation. However, the intensity of colors correlates within each measurement to the magnitude of segregation between elements. The brightest signal in the grain boundary of both samples originates from V, indicating strongest segregation of this element. This is followed



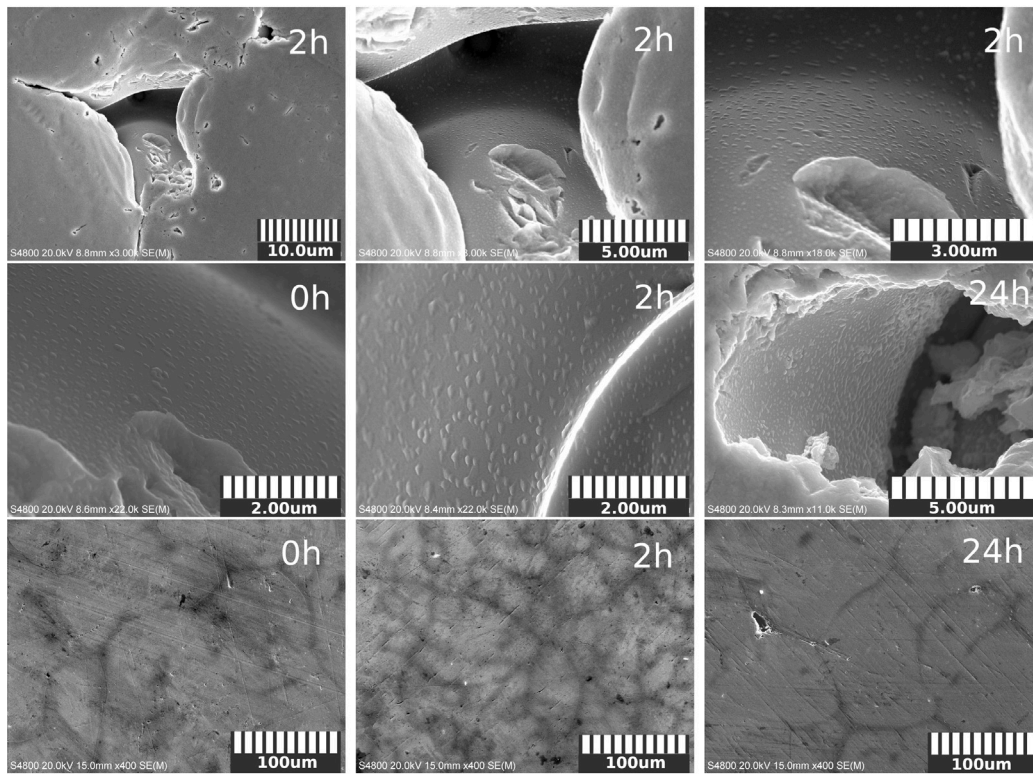


**Fig. 2.** Scanning electron microscopy images of WMoTaNbV alloy surface. Top row: The intergranular pore on the sample annealed for 2h and the spherical formations on the surface as imaged with increasing magnifications. Middle row: The morphologies covering inner surfaces of pores in samples that had undergone 0 h, 2 h and 24 h annealing periods, ordered from left to right, respectively. Bottom row: The grain-level microstructures of samples with 0 h, 2 h and 24 h annealings, ordered from left to right, respectively.

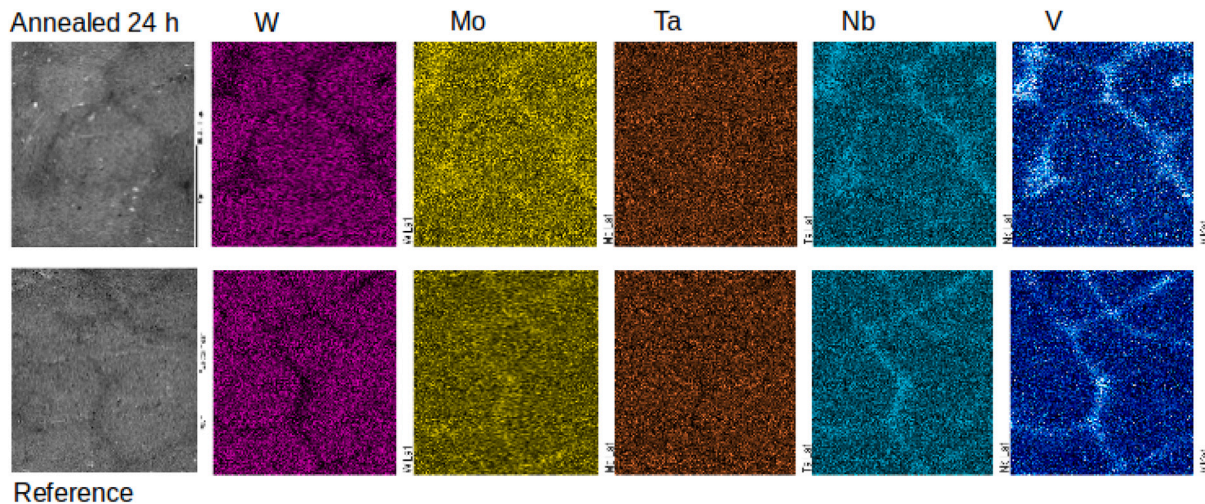


**Fig. 3.** Elemental maps of the WMoTaNbV sample annealed for 24 h and of the un-annealed reference sample, measured with energy dispersive spectroscopy.

by the intensity of Nb and then Mo signals at the boundary, marking a weaker segregation. The qualitative trend is consistent between the samples suggesting the segregation not being dramatically influenced by 1000 °C annealing, even over prolonged time periods, such as 24 h.

### 3.2. Elemental segregation and the effect of microstructure on H level

To study the degree of elemental segregation by sample, we have performed a series of EDS point measurements. To reduce statistical uncertainty, a total number of (7 + 7) point measurements were performed on each sample, probing the grain boundary and central parts of the grain. The measurements were normalized and analyzed in identical

manner to obtain quantitative analysis of the elemental compositions between the samples. The results, pictured in Fig. 4, show consistency with the elemental mappings of Fig. 3. In each of the sample the grain boundary is enriched with V, forming a concentration over 30 at. %. Similar trend is observed in Nb and Mo, which form approximately a quarter and one fifth of the boundaries' composition, respectively. Followed by even lower concentration of Ta and W, with latter having a proportion below 12 at. % of the elements at the boundary. The results are consistent throughout the sample set. The error margins related to Fig. 4 are obtained from the variance between measurements, implying a heightened variation in compositions of grain boundaries as compared to the innermost parts of the grain. The uncertainties along with the numerical values for elemental composition are presented

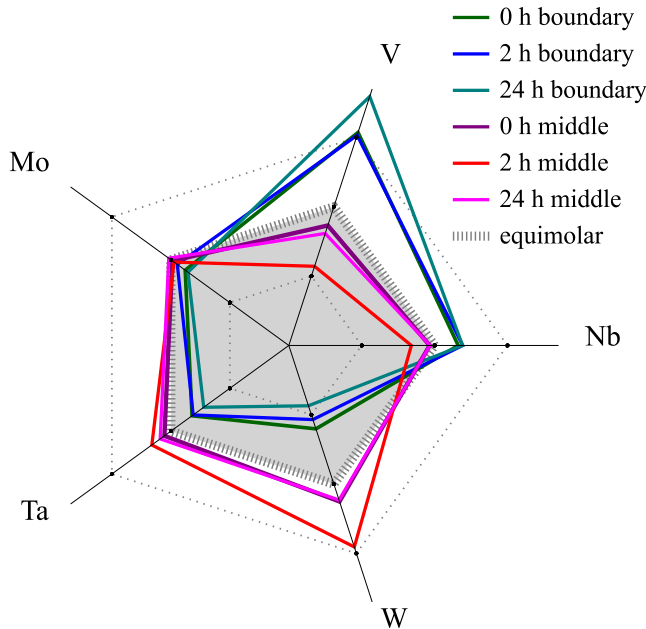


Fig. 4. The elemental compositions of the 0 h, 2 h and 24 h annealed samples as characterized by EDS point measurements. The values are displayed in Appendix along with error margins, indicating the variance in at. % as calculated from the statistics of 7 measurements composing each data point.

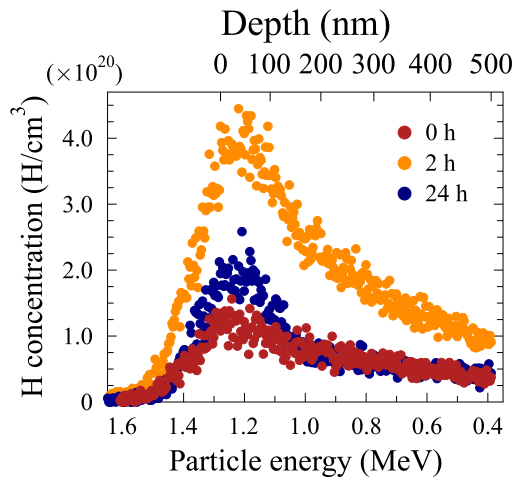


Fig. 5. The hydrogen depth profiles from surface level until depth of 500 nm, as measured by ERDA. The times in the figure refer to the annealing times of each sample before a yearlong H charging by exposure to ambient air.

in Appendix. These uncertainties are influenced by a smaller size of the region of interest and reflect the challenges in positioning of point measurement. The measurements performed on the middle parts of the grain show significantly smaller variation between individual zones of probing. In these regions the elemental composition is reverse, with W showing the highest percentage and V the lowest. The comparison between the compositions of each sample shows a similarity of their elemental proportions in the middle and in the boundary parts. The variations in Fig. 4 are likely related to natural variation between samples and unaffected by the annealing. The centers of the grains show a consistently smaller concentration of V, Nb and Mo as well as larger concentration of Ta and W.

However, the examination of the bottom row in the Fig. 2 reveals a significantly more refined microstructure in the 2 h annealed sample as compared to two others with a smaller grain size and by extension,

Table 1

The first column refers to times of annealing prior to H charging. The following columns present the average grain diameter and the hydrogen concentrations as characterized by ERDA. The depth profiles are presented in Fig. 5. Samples were loaded with hydrogen by being exposed to ambient air for a year. The levels of hydrogen are inversely correlated with the size of the grain. SEM images of grains are shown in the bottom row of Fig. 2.

Ann.	Grain diam.	H concentration
0 h	$120 \pm 25 \mu\text{m}$	$(0.44 \pm 0.01) \times 10^{16} \text{ cm}^{-2}$
2 h	$25 \pm 7 \mu\text{m}$	$(1.33 \pm 0.01) \times 10^{16} \text{ cm}^{-2}$
24 h	$90 \pm 12 \mu\text{m}$	$(0.54 \pm 0.01) \times 10^{16} \text{ cm}^{-2}$

higher density of pores between the grains. The coarse estimation of average grain sizes in the samples results in the average sizes of  $120 \pm 25 \mu\text{m}$ ,  $25 \pm 7 \mu\text{m}$  and  $90 \pm 10 \mu\text{m}$ , for 0 h, 2 h and 24 h annealed samples, respectively. The measured hydrogen concentrations from each sample are presented in the Table 1, and in Fig. 5, hydrogen depth profiles are shown until 500 nm in each sample. The results show that there is a correlation between the volumetric ratio of the grain boundary and hydrogen concentration in the WMoTaNbV alloy.

#### 4. Discussion

The accumulation of hydrogen in the samples with higher volumetric ratio of grain boundary can be attributed to the elemental segregation, as the boundaries are enriched specifically with hydrogen absorbing elements — V and Nb. Additionally, the segregation is more pronounced in samples with smaller grains, as the volumetric portion of the grain boundary becomes relatively larger. Therefore, the hydrogen distribution within the alloy is unlikely to be uniform but possibly shows some variation along the matrix, as guided by the local elemental compositions. Moreover, the intergranular pores occur in higher density in the samples with more refined microstructure. If the pores contribute to the uptake of hydrogen, the higher density may provide a network of absorption sites, adding to the efficiency of hydrogen absorption. In BCC metals, hydrogen is known to accumulate in the zones with elevated strain and stress fields, such as crack tips and plastic deformation [9]. The spherical formations on the grain surface imply an incomplete relaxation of the lattice structure, and are in themselves likely contribute to the formation of stresses. Due to even coverage of spherical formations on the intergranular pores, the effect on hydrogen absorption intensifies with more surface area inside the pore. In addition, the spherical formations are likely to have a different composition from the matrix, possibly enriched with one or more of the constituent elements as the morphology of the spherical formations is unaffected by annealing, similarly to the level of segregation. Additionally, the segregation is closely associated with grain structure, suggesting a lack of temperature-induced mobilization of V atoms in alloy. The qualitative trend is consistent between the samples suggesting the segregation not being dramatically influenced by 1000 °C annealing, even over prolonged time periods, such as 24 h. The stability under high temperature loads is advantageous considering the material applications in fusion.

#### 5. Conclusions

This study is a preliminary work investigating the impact of microstructure on hydrogen absorption to the WMoTaNbV alloy. The hydrogen absorption is connected to the grain size of the samples and may be driven by intergranular pores, by elemental segregation at the grain boundary or possibly via combination of these and other features of the alloy. Further research considering a larger variation of the grain sizes and different types of structural defects is valuable for better understanding of the mechanisms behind hydrogen absorption.

**Table A.1**

Normalized compositions in at. % at the grain boundary and center as characterized by EDS. The margin of error for the values indicates the variance in at. % as calculated from the statistics of 7 measurements composing each data point.

Bound.	0 h	2 h	24 h	Mid.	0 h	2 h	24 h
V	31 ± 7	30 ± 3	36 ± 3	V	17.3 ± 0.2	11.4 ± 0.6	16.2 ± 1.5
Nb	23.2 ± 0.7	23.9 ± 1.1	23.8 ± 0.6	Nb	19.3 ± 0.4	16.8 ± 0.6	19.4 ± 0.5
Mo	17.5 ± 1.1	18.9 ± 0.7	17.1 ± 1.0	Mo	19.8 ± 0.5	19.5 ± 0.5	20.4 ± 0.2
Ta	16 ± 3	16.2 ± 1.4	14.4 ± 1.2	Ta	21.1 ± 0.3	23.2 ± 0.3	21.8 ± 0.7
W	12 ± 5	10.7 ± 2.0	8.7 ± 1.4	W	22.5 ± 0.3	29.1 ± 1.3	22.3 ± 1.3

### CRedit authorship contribution statement

**Anna Liski:** Writing – review & editing, Writing – original draft, Visualization, Formal analysis, Data curation. **Marianna Kemell:** Writing – review & editing, Validation, Formal analysis, Data curation. **Tomi Vuoriheimo:** Writing – review & editing, Methodology. **Ko-Kai Tseng:** Resources. **Ting-En Shen:** Resources. **Che-Wei Tsai:** Resources. **Jien-Wei Yeh:** Resources. **Kenichiro Mizohata:** Writing – review & editing, Validation, Supervision, Project administration, Methodology, Investigation, Conceptualization.

### Declaration of competing interest

The authors declare that they have no known competing financial interests or personal relationships that could have appeared to influence the work reported in this paper.

### Acknowledgments

This work was financially supported by the “High Entropy Materials Center” from The Featured Areas Research Center Program within the framework of the Higher Education Sprout Project by the Ministry of Education (MOE) and from the Project NSTC 111-2634-F-007-008- and NSTC 112-2224-E-007-003 by National Science and Technology Council (NSTC) in Taiwan. This work has been carried out within the framework of the EUROfusion Consortium, funded by the European Union via the Euratom Research and Training Programme (Grant Agreement No 101052200 — EUROfusion). Views and opinions expressed are however those of the author(s) only and do not necessarily reflect those of the European Union or the European Commission. Neither the European Union nor the European Commission can be held responsible for them. SEM imaging and EDS measurements were performed in ALD center Finland research infrastructure.

### Appendix

See [Table A.1](#).

### Data availability

Data will be made available on request.

### References

- [1] E.J. Pickering, A.W. Carruthers, P.J. Barron, et al., High-entropy alloys for advanced nuclear applications, *Entropy* 23 (2021) 98.
- [2] Z.Q. Xu, Z.L. Ma, M. Wang, et al., Design of novel low-density refractory high entropy alloys for high-temperature applications, *Mater. Sci. Eng. A* 755 (2019) 318–322.
- [3] O.N. Senkov, G.B. Wilks, D.B. Miracle, et al., Refractory high-entropy alloys, *Intermetallics* 18 (2010) 1758–1765, <http://dx.doi.org/10.1016/j.intermet.2010.05.014>.
- [4] A. Liski, T. Vuoriheimo, P. Jalkanen, et al., Irradiation damage independent deuterium retention in WMoTaNbV, *Mater.* 17 (2024) 2574, 11.
- [5] T. Vuoriheimo, A. Liski, P. Jalkanen, et al., Hydrogen isotope exchange experiments in high entropy alloy WMoTaNbV, *Nucl. Mater. Energy* 34 (2023) 101348.
- [6] A. Liski, T. Vuoriheimo, J. Byggmästar, et al., Solubility of hydrogen in WMoTaNbV high-entropy alloy, *Materials* 19 (2024) 698–706.
- [7] X.L. Ren, P.H. Shi, B.D. Yao, et al., Hydrogen solution in high-entropy alloys, *Phys. Chem. Chem. Phys.* 23 (2021) 27185.
- [8] M. Sahlberg, D. Karlsson, C. Zlotea, et al., Superior hydrogen storage in high entropy alloys, *Sci. Rep.* 6 (2016) 36770.
- [9] T. Cui, H. Dong, X. Xu, et al., Hydrogen-enhanced oxidation of ferrite phase in stainless steel cladding and the contribution to stress corrosion cracking in deaerated high temperature water, *J. Nucl. Mater.* 557 (2021) 153209.
- [10] K.-K. Tseng, C.-C. Juan, S. Tso, et al., Effects of Mo, Nb, Ta, Ti, and Zr on mechanical properties of equiatomic Hf-Mo-Nb-Ta-Ti-Zr alloys, *Entropy* 21 (2018) 15.
- [11] O.N. Senkov, G.B. Wilks, J.M. Scott, et al., Mechanical properties of Nb<sub>25</sub>Mo<sub>25</sub>Ta<sub>25</sub>W<sub>25</sub> and V<sub>20</sub>Nb<sub>20</sub>Mo<sub>20</sub>Ta<sub>20</sub>W<sub>20</sub> refractory high entropy alloys, *Intermetallics* 19 (2011) 698–706.